Influence of a magnetic field on liquid metal free convection in an internally heated cubic enclosure

Michele Ciofalo and Fabrizio Cricchio
Dipartimento di Ingegneria Nucleare, Università di Palermo, Viale delle Scienze, Palermo, Italy

Keywords *Hydromagnetics, Natural convection, Buoyancy, Fluid, Metals*

Abstract *The buoyancy-driven magnetohydrodynamic flow in a cubic enclosure was investigated by three-dimensional numerical simulation. The enclosure was volumetrically heated by a uniform power density and cooled along two opposite vertical walls, all remaining walls being adiabatic. A uniform magnetic field was applied orthogonally to the gravity vector and to the temperature gradient. The Prandtl number was 0.0321 (characteristic of Pb–17Li at 300°C), the Rayleigh number was 10^4, and the Hartmann number was made to vary between 0 and 2×10^3. The steady-state Navier–Stokes equations, in conjunction with a scalar transport equation for the fluid's enthalpy and with the Poisson equation for the electrical potential, were solved by a finite volume method using a purposely modified CFD code and a computational grid with 64^3 nodes in the fluid. Emphasis was laid on the effects of increasing the Hartmann number on the complex three-dimensional flow and current pattern.*

Nomenclature

$\mathbf{B}$ = magnetic induction vector
c_p = specific heat
c_w = wall conductance ratio, $(\sigma_w s_w)/(\sigma D)$
D = side length of the enclosure
$\mathbf{g}$ = gravity vector
$\mathbf{J}$ = electrical current density vector
M = Hartmann number, $DB\,(\sigma/\mu)^{1/2}$
N = interaction parameter, $(\sigma DB^2)/(\rho U_0)$
Pr = Prandtl number, ν/α
p = difference between local and hydrostatic pressure
q = thermal power density
q'' = surface heat flux
Ra = Rayleigh number, $g\beta\Delta T D^3/(\nu\alpha)$
$\mathrm{Re_m}$ = magnetic Reynolds number, $U_0 D\sigma\eta$
s = thickness
t = time
T = difference between local and cold wall temperature
U_0 = velocity scale, α/D
u, v, w = velocity components
$\mathbf{v}$ = velocity vector
x, y, z = cartesian co-ordinates

Greek

α = thermal diffusivity, $\lambda/(\rho c_p)$
β = thermal expansion coefficient
δ = thickness of the Hartmann layers
ΔT = reference temperature difference, qD^2/λ
η = magnetic permeability
λ = thermal conductivity
μ = viscosity
ν = kinematic viscosity, μ/ρ
ρ = density
σ = electrical conductivity
τ = shear stress
Φ = electrical potential

Subscripts

w = solid wall
0 = reference value for scaling

International Journal of Numerical Methods for Heat & Fluid Flow, Vol. 12 No. 6, 2002, pp. 687-715.

DOI 10.1108/09615530210438355

1. Introduction and review of the literature

Free convection magnetohydrodynamic (MHD) flow is encountered in a number of problems of engineering and physical interest, ranging from geophysics to metallurgy, crystal growth technology and nuclear engineering (Moreau, 1990).

As will be discussed later, forced MHD flows are often dominated by a relatively simple balance between pressure gradients and MHD forces (Müller and Bühler, 2001). Buoyant MHD flows usually present a greater complexity and buoyant, viscous, inertial and MHD forces all play a role. Analytical and asymptotic solutions are known only for the simplest geometrical configurations, with special reference to those cases in which the problem can be reduced to a two-dimensional one (Bühler, 1996; 1998; Alboussière *et al.*, 1996). Interestingly, forced and buoyant MHD flows, respectively, occur in the two main designs currently being considered for the breeder blanket of fusion nuclear reactors, namely, the self-cooled concept (Malang and Tillack, 1995) and the separately-cooled concept (Proust *et al.*, 1993).

Three-dimensional numerical simulations of buoyant MHD flow in a differentially heated cubic enclosure were presented by Tagawa and Ozoe (1997). The Prandtl number was 0.025, the Rayleigh number (based on the side length D and on the imposed temperature difference ΔT) was either 10^5 or 10^6, and the Hartmann number M ranged from 0 to 10^3; the surrounding solid walls were assumed to be electrically nonconducting. The magnetic field was orthogonal to the temperature gradient and to the gravity vector, as in the present work. The authors used a time-dependent, finite difference method based on staggered grids with up to 46^3 nodes, which were mildly refined towards the walls. The predicted flow was unsteady up to $M \approx 100$ in the case $\mathrm{Ra} = 10^5$, and for all values of M in the case $\mathrm{Ra} = 10^6$. A slight enhancement of heat transfer rates (of the order of a few per cent) was predicted for moderate Hartmann numbers, maximum values being attained for $M = 50-100$. This phenomenon was explained by the authors as resulting from the "flow rectifying" effect of MHD, i.e. from the flattening of the vertical velocity profiles near the thermally active walls in the presence of a magnetic field. These computational findings were supported by subsequent experimental studies conducted in liquid gallium-filled enclosures (Tagawa and Ozoe, 1998a).

In further work, Tagawa and Ozoe (1998b) investigated the influence of the electrical conductivity of the surrounding walls. The geometry (differentially heated cubic enclosure) and the Prandtl number (0.025) were the same as in their 1997 paper, the Rayleigh number was $\mathrm{Ra} = 10^5$, and the Hartmann number was 0 or 100; the finite-difference grid included just 32^3 nodes, of which only 22^3 were located in the fluid and the remaining ones in the solid walls. The authors found that, when the magnetic field was orthogonal to the temperature gradient, convective flow and heat transfer were significantly suppressed at $M = 100$ only if the walls were well conducting (conductivity ratio

$c_w = (\sigma_w s_w)/(\sigma D) \approx 0.1$ in the present notation), whereas they were little affected for lower values of c_w. On the other hand, a magnetic field parallel to the temperature gradient was much more effective in suppressing convection even at low values of c_w. For c_w larger than ~ 1, the direction of the magnetic field had very little influence on the overall heat transfer rates.

Di Piazza (2000) presented a general approach to MHD problems, based on the implementation of appropriate terms describing the MHD interactions into a general-purpose CFD code, CFX-4 (AEA Technology, 2000). In order to allow comparisons with existing analytical solutions, applications were first presented for a highly simplified geometry, i.e. fully developed buoyant flow in a vertical duct of square cross section, which is essentially a two-dimensional problem (Di Piazza and Bühler, 2000). In later work (Di Piazza and Ciofalo, 2002a, b), the same modified code was applied to a more complex and fully three-dimensional problem (buoyant MHD flow in a differentially or internally heated cubic enclosure), for which no analytical solution exists.

However, even in these latter applications some limitations were present, which hindered the straightforward extension of the method to more general geometries, notably involving curved surfaces. In particular, this regarded the treatment of the Hartmann layers, thin fluid layers which develop over solid walls orthogonal to the magnetic field, and in which most of the velocity gradient is concentrated. Following Leboucher (1995, 1999) the Hartmann layers were given an *ad hoc* treatment (HLA approach), which was to include their electric conductance into that of the solid bounding walls, while simultaneously replacing the exact no-slip velocity boundary conditions with free-slip ones. This technique permits one to avoid the fine discretization of the near-wall Hartmann region, with consequent savings in grid size and computational effort; however, it meets with difficulties in the presence of walls which lie neither parallel nor orthogonal to the applied magnetic field, and, *a fortiori*, in the presence of curved walls. Moreover, the method cannot be applied to problems characterized by a low value of the Hartmann number, e.g. by the presence of a weak magnetic field, since in this case the Hartmann layers become thick and may cover a significant fraction of the whole computational domain. The situation is somehow similar to that encountered in the numerical simulation of turbulence, when models based on "wall functions" must be replaced by low-Reynolds number models in the case of transitional and weakly turbulent flows (Ciofalo and Collins, 1989).

In Ciofalo and Cricchio (2001), the *ad hoc* treatment of the Hartmann layers was compared with the more general, "direct" method (HLD approach), based on their resolution by the computational grid. In order to reduce the computational effort, and to draw comparisons with results in Bühler (1998) and Di Piazza and Bühler (2000), only the two simple configurations studied therein (fully developed flow in a vertical square duct with differential or internal heating) were simulated. Results showed that HLD simulations with 64

or more grid points along the magnetic field direction (five or more of which lying within the Hartmann layer) satisfactorily reproduced the flow and electric potential distributions computed by the *ad hoc* HLA approach, while at the same time resolving (rather than postulating) the sharp velocity gradients which occur in the near-wall regions. In further work (Ciofalo and Cricchio, 2002) the comparison between the two approaches was extended, with similar results, to fully three-dimensional buoyant flow in a cubic enclosure with either differential or internal heating.

In the present work, only the "direct" HLD approach was used and emphasis was laid on the influence of a weak magnetic field, including values of the Hartmann number as low as 1. This allowed a better understanding of the incipient modifications of the base flow caused by MHD effects and of the scaling laws which apply to low-M flows, as opposed to high-M, MHD-dominated, problems.

Only a low value of the Rayleigh number (10^4) was considered so that the base flow obtained for $M = 0$ was steady and symmetric. In fact, simulations conducted for $\mathrm{Ra} = 10^5$ yielded an *asymmetric* steady-state solution at $M = 0$. The possibility that the base, symmetric flow predicted for low values of Ra in an internally heated cubic enclosure at $M = 0$ may break down at Rayleigh numbers higher than $\sim 10^4$, giving rise to either steady but asymmetric, or even unsteady, flow patterns, is also suggested by several previous studies. For example, Arcidiacono *et al.* (2001) conducted high-resolution two-dimensional, time-dependent simulations for internally heated square enclosures at the same Prandtl number (0.0321) and found that the base symmetric flow was stable only up to $\mathrm{Ra} \approx 3 \times 10^5$; for $\mathrm{Ra} = 10^6$ the stable flow configuration was steady but asymmetric and, for $\mathrm{Ra} = 1.7 \times 10^6$, transition to time-periodic flow occurred, while chaotic flow was obtained for even higher values of Ra ($\sim 3 \times 10^6$). Since three-dimensional free convection flows are known to be more unstable than two-dimensional ones (Henkes and Le Quéré, 1996), the upper limits of existence of the steady symmetric base flow in the absence of MHD effects may well be of the order of $\mathrm{Ra} = 10^5$ for the internally heated cubic enclosure. Similar limits are suggested also for *differentially* heated enclosures by the numerical simulations of Tagawa and Ozoe (1997), who, as mentioned above, found unsteady flow at $\mathrm{Ra} = 10^5$ not only for the base case $M = 0$ but even in the presence of MHD effects up to $M \approx 100$.

2. Model and computational methods

The configuration studied (internally heated cubic enclosure) is shown in Figure 1, where also the nomenclature adopted for the co-ordinate axes are shown. A fluid of density ρ, viscosity μ, specific heat c_p, thermal conductivity λ and electrical conductivity σ fills a cubic cavity of side length D, surrounded by a solid wall of thickness s_w and electrical conductivity σ_w.

The main dimensionless parameters which characterize the present problem are the Prandtl number $\mathrm{Pr} = c_p\mu/\lambda$, the wall conductance ratio $c_w = (\sigma_w s_w)/(\sigma D)$, the Rayleigh number Ra and the Hartmann number M.

Here, the Rayleigh number can be defined as

$$\mathrm{Ra} = g\beta\Delta T D^3/(\nu\alpha) \tag{1}$$

where β, $\nu = \mu/\rho$ and $\alpha = \nu/\mathrm{Pr}$ are the fluid's thermal expansion coefficient, kinematic viscosity, and thermal diffusivity, respectively. Following previous work (Ciofalo and Cricchio, 2001), the reference temperature difference is conventionally taken as $\Delta T = qD^2/\lambda$.

The Hartmann number is defined as

$$M = DB(\sigma/\mu)^{1/2} \tag{2}$$

and represents the square root of the ratio between electromagnetic and viscous forces. The walls normal to **B** are called *Hartmann walls*; in the corresponding boundary layers, the velocity profile is determined by a balance between Lorentz and viscous forces. It has been shown that, in the limit of large M, their thickness scales as M^{-1}. The walls parallel to the magnetic field are called *side walls*, and the corresponding boundary layers are called *side layers*; for large M, their thickness scales as $M^{-1/2}$.

Another important dimensionless number is the interaction parameter $N = (\sigma DB^2)/(\rho U_0)$, in which U_0 is a characteristic velocity scale. For the present, low-Rayleigh number, free convection problem this latter can be identified with the diffusive velocity scale α/D; therefore, taking into account the above definition of the Hartmann number M, one simply has $N = M^2\mathrm{Pr}$. The interaction parameter characterizes the ratio of electromagnetic to inertial forces; for large values of N these latter (associated with the convection terms in the Navier–Stokes equations) can be neglected, and the problem depends on the balance between electromagnetic or buoyant forces and driving pressure

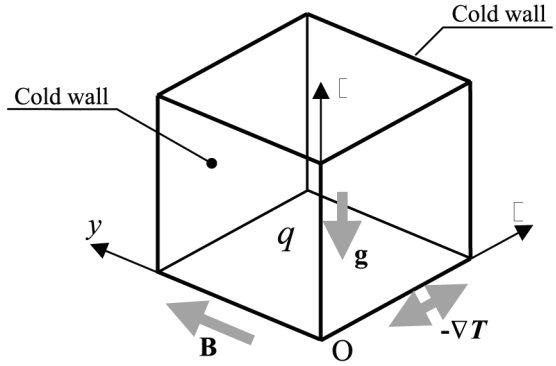

Figure 1.
Sketch of the internally heated cubic enclosure. The nomenclature used for the co-ordinate axes are also shown

gradients in the core, with an additional role for viscous resistances in the wall regions only (Hartmann and side layers). This makes it possible to adopt simplified asymptotic methods in which separate solutions are sought for the core and the near-wall flow and are then matched to yield the overall flow field (Bühler, 1998). In the present case ($\mathrm{Pr} = 0.0321$), one has $N = 1$ for $M \approx 5.6$, so that inertial terms can be expected to play a minor role only for M much larger than $5 \sim 10$.

Finally, a last relevant parameter is the magnetic Reynolds number $\mathrm{Re_m} = U_0 D\sigma\eta$, in which η is the fluid's magnetic permeability. The magnetic Reynolds number characterizes the ratio of induced to applied magnetic induction fields (Moreau, 1990). In the present case, by assuming again $U_0 = \alpha/D$ and using the properties of Pb–17Li, one has $\mathrm{Re_m} = \alpha\sigma\eta \approx 10^{-5}$. For such low values of $\mathrm{Re_m}$, the *induced* magnetic field is negligible with respect to the *applied* field **B**, which therefore coincides with the *total* field, and the flow is governed by momentum (Navier–Stokes) equations in which the Lorenz force $\mathbf{J} \times \mathbf{B}$ (**J** being the current density vector) is added among the source terms.

Summarizing, in the present work the assumption $\mathrm{Re_m} \ll 1$ (negligible induced magnetic field) is adopted, but the assumption $N \gg 1$ (negligible inertial terms) is not. By using the Boussinesq approximation for buoyancy and assuming steady-state conditions, the Navier–Stokes and continuity equations become

$$\rho(\mathbf{v}\cdot\nabla)\mathbf{v} = -\nabla p + \mu\nabla^2\mathbf{v} + \mathbf{J} \times \mathbf{B} - \rho\beta T\mathbf{g} \tag{3}$$

$$\nabla\cdot\mathbf{v} = 0 \tag{4}$$

Here, **v** is the velocity vector (u, v, w), p is the difference between the local and the hydrostatic pressure and T is the difference between the local temperature and the reference value for which the density value ρ holds. This reference value can be identified, without loss of generality, with the temperature of the cold walls.

For the current density **J**, Ohm's law and the principle of conservation of the electric charge lead to

$$\mathbf{J} = \sigma(\mathbf{v} \times \mathbf{B} - \nabla\Phi) \tag{5}$$

$$\nabla\cdot\mathbf{J} = 0 \tag{6}$$

For uniform **B**, from equations (5) and (6) the following Poisson equation for the electrical potential Φ is obtained:

$$\nabla^2\Phi = (\nabla \times \mathbf{v})\mathbf{B} \tag{7}$$

The temperature distribution is governed by the enthalpy transport equation:

$$\rho c_p(\mathbf{v}\cdot\nabla)T = \lambda\nabla^2 T + q \tag{8}$$

The velocity boundary conditions are those of no-slip at the walls, while the thermal boundary conditions are:

$$T = 0 \qquad \text{at } x = 0 \text{ and } x = D \tag{9}$$

Continuity of Φ and $\mathbf{J}$ is imposed at the fluid-wall interface, and the condition $\mathbf{J}\cdot\mathbf{n} = 0$ of zero normal current at the outer surface of all solid walls.

Whenever results for MHD and non-MHD flows have to be compared, the present formulation of the governing equations is preferable to the dimensionless form used, for example, in Di Piazza and Bühler (2000) or in Ciofalo and Cricchio (2001), which was based on magnetic scales; these latter, in fact, become meaningless for $M = 0$ (no MHD).

The choice of the computational domain and the related issue of the problem's symmetries deserve a brief mention. First, it should be observed that the problem is apparently symmetric with respect to the mid-plane $x/D = 0.5$, parallel to $\mathbf{B}$ and located midway between the two thermally active walls. However, this symmetry holds only for the velocity and temperature fields but not for the electric quantities; as will be shown in Section 5, electric currents exhibit a different symmetry and actually *cross* the above mid-plane, so that reducing the computational domain to either half of the regions in which this plane divides the cavity is not feasible.

More complex is the case of the plane $y/D = 0.5$, orthogonal to $\mathbf{B}$ and located midway between the two Hartmann walls. Although this is not a global symmetry plane for the present problem (since one of the quantities involved, the magnetic field $\mathbf{B}$, crosses this plane and is not symmetric with respect to it), it can be shown by an analysis of the governing equations (and it is confirmed by the computational results) that y-symmetric solutions exist *both* for the flow and thermal fields and for the electrical quantities. Therefore, in principle the computational domain might have been restricted to either of the regions in which the plane $y/D = 0.5$ divides the cavity, with symmetry conditions imposed on it to velocities, temperature, electric currents and electric potential. However, as mentioned in Section 1, the possibility of symmetry breaking leading to y-asymmetric solutions suggested to avoid also for this direction the recourse to simplifying symmetry assumptions. Thus, in the end the computational domain was chosen to include the whole of the cubic enclosure.

Equations (3), (4), (7) and (8) were solved by the CFX-4 computer code (AEA Technology, 2000). The code is based on a finite volume method which allows for general body-fitted grids (Burns and Wilkes, 1987), although, of course, only simple orthogonal grids were required for the present simulations. A co-located grid approach is adopted, i.e. all variables are defined at the centers of the control volumes, and the Rhie and Chow (1983) algorithm is used to prevent "chequerboard" oscillations. Pressure–velocity coupling was performed by means of the SIMPLEC algorithm (Van Doormal and Raithby, 1984); the second-order central discretization scheme was adopted for the diffusive terms,

and the third-order QUICK scheme (Leonard, 1979) for the convective terms. At each "outer" SIMPLEC iteration, the linearized equations were solved by using a three-dimensional version of Stone's (1968) "strongly implicit" procedure, with the exception of the pressure-correction equation which was solved by a preconditioned conjugate gradient method (Kightley, 1985). Steady-state conditions were always imposed, and moderate under-relaxation factors (0.85 or larger) were used for all variables.

Following preliminary tests, a grid of 64^3 nodes in the fluid, selectively refined towards the walls, proved to yield an almost complete grid-independence of the results.

In all cases, the residuals of all equations decreased monotonically for 1000–3000 iterations until they attained final values which were 3–4 orders of magnitude smaller than those characteristic of the first few iterations; convergence was somewhat slower at high-Hartmann numbers than at low-Hartmann numbers. Following this monotonical convergence, residuals started to fluctuate around their low final values, while flow and electrical quantities at selected monitoring points exhibited no further significant variations between subsequent iterations. Computations were halted at this stage; corresponding CPU times were of the order of 10 h per test case on a 1500-MHz PC with 512 MB RAM.

Special adaptations of the code were required since it does not explicitly provide for MHD problems; in particular, the electrical potential equation was solved by using the elliptic solvers normally adopted for the solution of scalar transport equations, modified so as not to include convection terms. Further details have been given by Di Piazza (2000).

In the present simulations, the Prandtl number was 0.0321, the Rayleigh number was set to 10^4 (for the reasons discussed above), and the wall conductance ratio c_w was set to 0.01. More specifically, the cavity side length was assumed to be 0.01 m and the physical properties of the Pb–17Li lithium–lead eutectic ($\beta = 1.8 \times 10^{-4}\,\mathrm{K}^{-1}$, $\rho = 9400\,\mathrm{kg/m^3}$, $\mu = 2.2 \times 10^{-3}\,\mathrm{Pa\,s}$, $\lambda = 13\,\mathrm{W/(m\,K)^1}$, $\sigma = 7.3 \times 10^5\,\Omega\,\mathrm{m}^{-1}$) were used for the fluid, which was assumed to be surrounded by a 0.1 mm thick solid wall having an electric conductivity equal to σ. The power density was thus $\sim 12.6\,\mathrm{kW/m^3}$. Different values were imposed for the Hartmann number M; results will be presented here for M ranging from 1 to 2000, in addition to the purely hydrodynamic case $M = 0$. The value $M = 2000$ corresponds to a magnetic induction field of ~ 1.1 T.

In all cases, solid bounding walls were assumed to be electrically insulated on their outer surfaces and were resolved by just one grid point in the normal direction. Thermal boundary conditions were directly imposed at the fluid–solid interface, so that heat conduction in the solid did not have to be modelled.

Most results will be shown in dimensionless form using the following scales, all chosen in such a way that they depend only on the side length D and on the

physical properties of the fluid, but not on the magnetic field:

• Length	D	(side length of the enclosure)
• Velocity	$U_0 = \alpha/D$	(diffusive velocity scale)
• Time	$t_0 = D^2/\alpha$	(diffusive time scale)
• Temperature	$\Delta T/8 = (qD^2)/(8\lambda)$	(conductive temperature maximum)
• Heat flux	$qD/2$	(average heat flux)
• Current density	$J_0 = (\mu\sigma)^{1/2}\alpha/D^2$	
• Electrical potential	$(\mu/\sigma)^{1/2}\alpha/D$	
• Pressure and shear stress	ρU_0^2	

3. Results for $M = 0$ (no MHD)

First, computational results will be presented for the case $M = 0$ (no MHD). Figure 2(a) shows the in-plane velocity vector plot in the vertical mid-plane $y/D = 0.5$, parallel to the Hartmann walls. As could be expected, the main flow pattern in this section (and in all the constant-y sections parallel to it) consists of two symmetric rolls, delimited by a central rising plume and by two boundary layers descending along the thermally active walls. A reference vector of length $10\,U_0$ is reported above the figure; it can be observed that all velocities are of the order of U_0 at the present, moderate Rayleigh number.

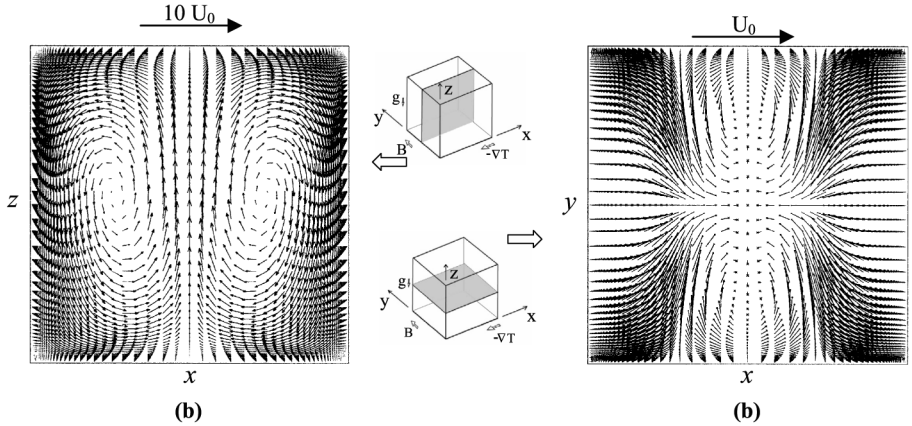

Figure 2.
In-plane velocity vector plots in selected cross-sections of the enclosure for $M = 0$ (no MHD). (a) vertical mid-plane $y/D = 0.5$; (b) horizontal mid-plane $z/D = 0.5$. Reference vectors are shown above each graph

However, a significant secondary flow is also present in the enclosure, as shown by Figure 2(b) which reports the in-plane velocity vector plot relative to the horizontal mid-plane $z/D = 0.5$. The fluid moves from the corners of this section towards the center of the enclosure, where it is entrained in the central uprising plume. A reference vector of length U_0 is reported above the figure; secondary velocities are about one order of magnitude smaller than the main velocities in Figure 2(a).

The overall three-dimensional flow pattern can be better appreciated by considering the axonometric views of particle trajectories shown in Figure 3. These were obtained by visualizing some 2000 consecutive positions of two pseudo-particles, moving along with the fluid and released at $t = 0$ from two arbitrary locations, close to the front wall $y = 0$ and symmetric about the cavity mid-plane $x/D = 0.5$. Graphs (a) and (b) show two alternative views of the same trajectories for $0 \leq t \leq 3D^2/\alpha^1$, while graphs (c) and (d) are relative to the subsequent time interval $3D^2/\alpha^1 \leq t \leq 7D^2/\alpha^{-1}$ (trajectories were split into two parts for the sake of clarity). The fluid moves from the front wall to the mid-plane $y/D = 0.5$ of the enclosure along lines close to the axes of the

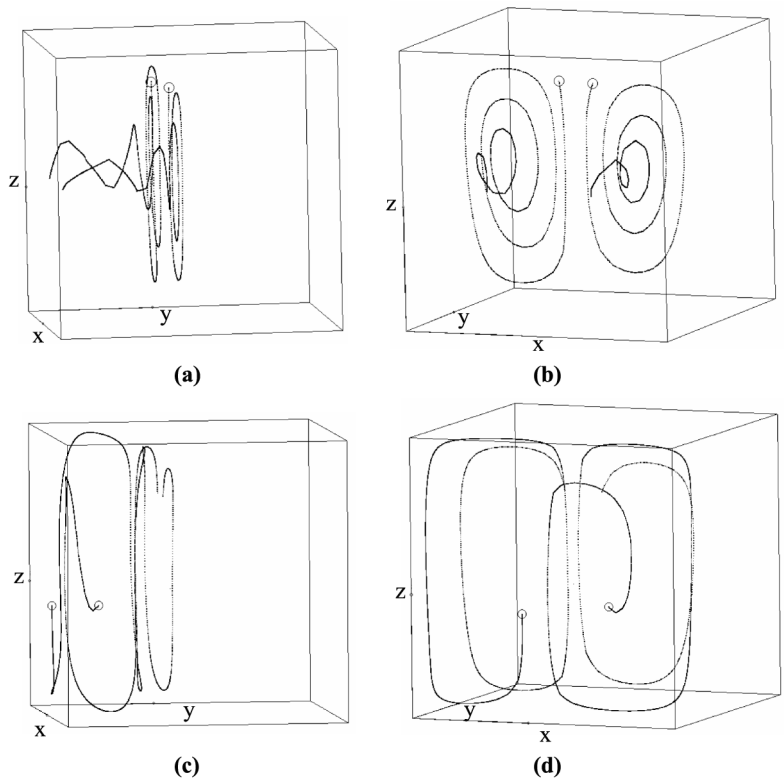

Figure 3.
Trajectories of two pseudo-particles for $M = 0$ (no MHD). (a, b) alternative axonometric views for $0 \leq t \leq 3D^2\,\alpha^{-1}$; (c, d) alternative axonometric views for $3D^2\,\alpha^{-1} \leq t \leq 7D^2\,\alpha^{-1}$. The starting co-ordinates of the two particles are $x/D = 0.3$, $y/D = 0.05$, $z/D = 0.5$ (P1) and $x/D = 0.7$, $y/D = 0.05$, $z/D = 0.5$ (P2). Small circles indicate the final positions

main circulation rolls, winds outward and comes back towards the front wall in ample spirals. Of course, a similar and symmetric pattern could be observed for particles starting from the opposite, back wall $y = D$.

Taking into account the different physical and boundary conditions, these flow patterns are coherent with those predicted, for example, by Mallinson and de Vahl Davis (1977) for the case of three-dimensional differentially heated enclosures; in this latter case, of course, patterns were simpler since they involved only a single main circulation cell.

The temperature distributions in the two cross sections $y/D = 0.5$ and $z/D = 0.5$ (corresponding to the velocity plots in Figure 2) are shown in Figure 4(a) and (b), respectively. Values are normalized with respect to $(qD^2)/(8\lambda)$, which is the maximum temperature that would be attained in the case of pure conduction (zero Prandtl number). It can be observed that, at the present moderate Rayleigh number, peak temperatures are only slightly lower than conductive ones, and that temperature depends mainly upon the horizontal direction as under pure conduction conditions; a moderate vertical thermal stratification is observed only in the central region of the enclosure ($x/D \approx 0.5$). As Figure 4(b) shows, the active secondary flow shown in Figure 2(b) has only a marginal influence on the temperature distribution, which exhibits almost parallel isotherms in the horizontal mid-plane. Of course, this is due to the low-Prandtl number of the fluid ($\mathrm{Pr} = 0.0321$). On the whole, the present conditions are not far from the limiting case of a zero-Prandtl number fluid, in which convection would have no influence at all on the temperature distribution.

Figure 5 shows the distributions of local heat flux q''_{w} (a) and total wall shear stress τ_{w} (b) along one of the side (thermally active) walls. The distributions are, of course, identical on the two cold walls at $x = 0$ and $x = D$. The heat flux is normalized by its average value $qD/2$, while the wall shear stress is normalized by ρU_0^2.

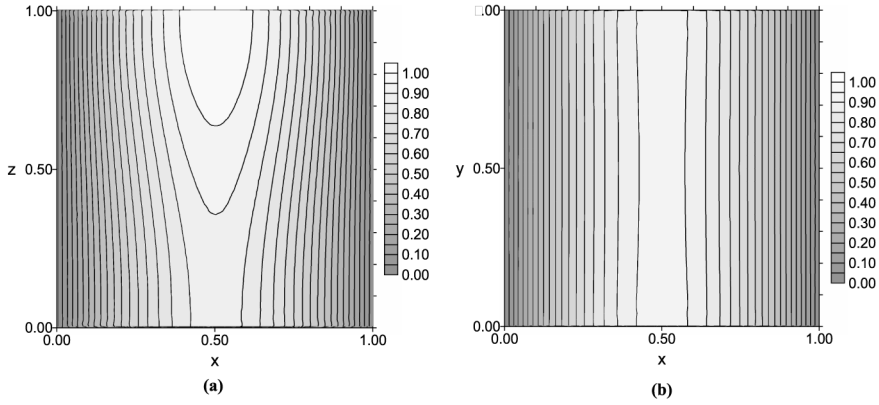

Figure 4. Temperature distributions in selected cross-sections of the enclosure for $M = 0$ (no MHD). (a) vertical mid-plane $y/D = 0.5$; (b) horizontal mid-plane $z/D = 0.5$. Temperatures are made dimensionless with respect to $(qD^2)/(8\lambda)$ (maximum conductive temperature)

Three-dimensional end effects due to the front and back walls are more pronounced than on the bulk temperature distribution, e.g. Figure 4(b). Peak values of the wall heat flux do not correspond to peak values of the wall shear stress; the former are attained very close to the upper end of the side walls, while the latter are shifted considerably downward ($z/D \approx 2/3$). As could be expected in view of the low-Prandtl number, the shear stress distribution is much less uniform than that of the heat flux; the corresponding peaking factor (ratio of maximum to average values) is ~ 2 for τ_w and only ~ 1.1 for q''_w.

4. Influence of magnetohydrodynamics on the flow and temperature fields

The influence of an external, uniform magnetic induction field **B** on convective flow patterns and temperature distributions will now be considered.

First, Figure 6 compares in-plane velocity vector plots for four values of the Hartmann number, namely, $M = 10$, 30, and 100 and 1000. The graphs on the left show the main, two-cell, flow in the vertical mid-plane $y/D = 0.5$, while those on the right refer to the secondary flow in the horizontal mid-plane at $z/D = 0.5$. A reference vector, proportional to the velocity scale U_0, is shown above each graph. The scale changes from graph to graph so that the largest vectors have roughly the same length, since the qualitative comparison of flow patterns, rather than the quantitative comparison of velocity values, is mainly addressed here. Corresponding cross-sections for the case $M = 0$ (no MHD) are shown in Figure 2.

Both main and secondary flow patterns are little affected by MHD effects at low-Hartmann numbers (e.g. $M = 10$, graphs (a)–(b)). At higher M the main circulation cells become more "square" as the flow tends to follow the boundaries of the enclosure. At the same time, in the horizontal planes

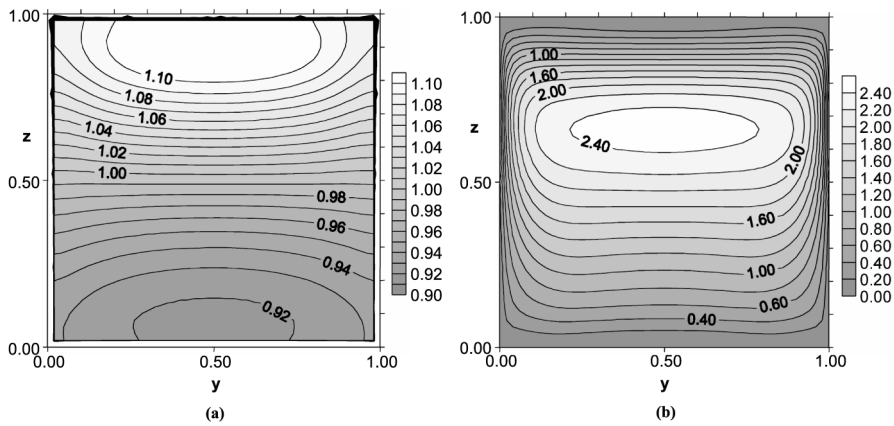

Figure 5.
Distributions of wall heat flux and wall shear stress on one of the side (thermally active) walls for $M = 0$ (no MHD). (a) wall heat flux q''_w, normalized by its mean value $qD/2$; (b) wall shear stress τ_w, normalized by ρU_0^2

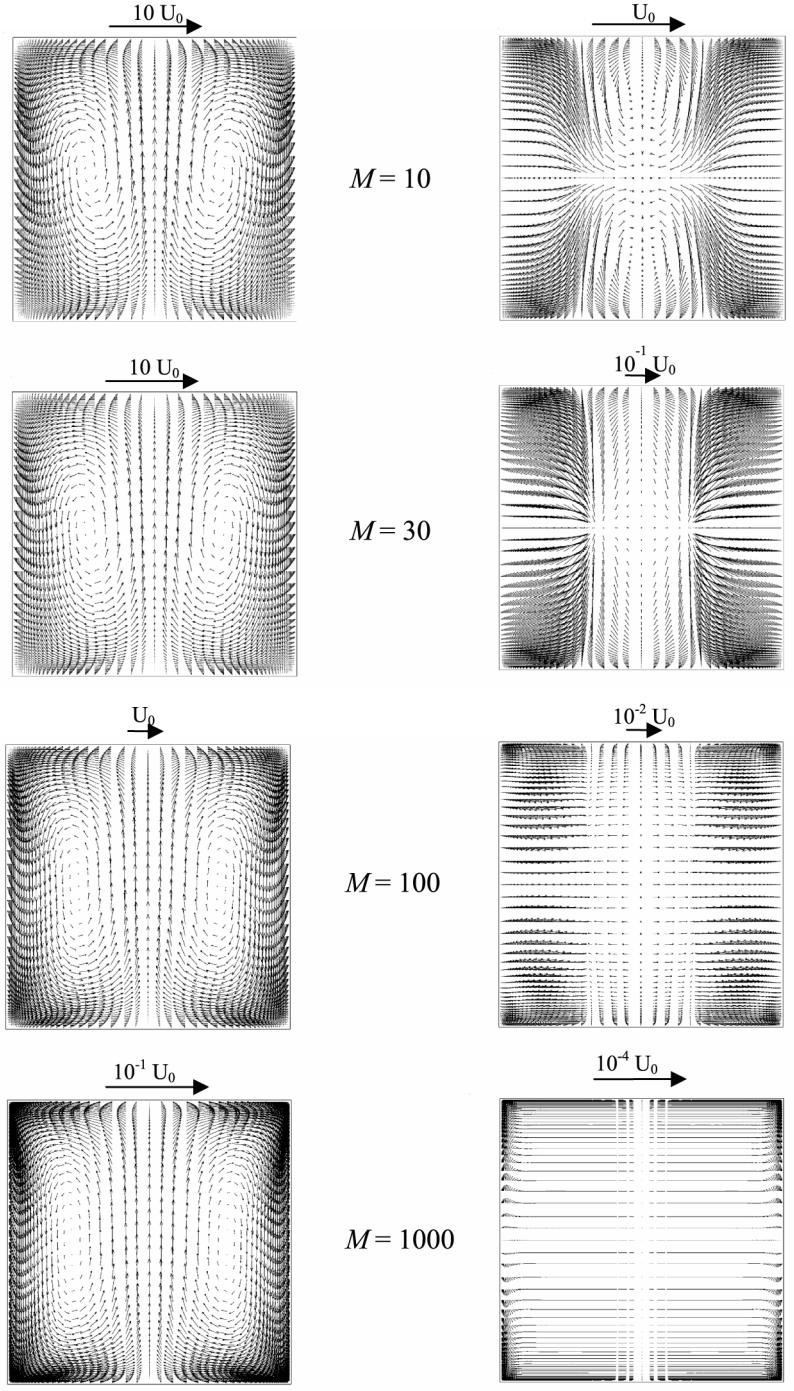

Figure 6.
In-plane velocity vector plots in selected cross-sections of the enclosure for different values of the Hartmann number. Left: vertical mid-plane $y/D = 0.5$; right: horizontal mid-plane $z/D = 0.5$. Reference vectors are shown above each graph

secondary velocities decrease considerably in module and tend to align themselves with the direction of the temperature gradient (i.e. orthogonal to the magnetic field); four distinct regions appear, alternately characterized by inward- and outward-directed secondary velocities. At high-Hartmann numbers (e.g. $M = 1000$) secondary flows become negligible while the tendency of the main flow to follow the enclosure boundaries become more pronounced.

A better quantitative comparison of convective velocities at different values of M can be drawn by considering Figure 7. Graph (a) shows profiles of the vertical velocity w along x (i.e. between the two thermally active walls) for $y/D = z/D = 0.5$, while graph (b) shows corresponding profiles along y (direction of the magnetic field) for $x/D = z/D = 0.5$. Values of w are normalized by the diffusive velocity scale $U_0 = \alpha/D$.

It can be observed that w profiles remain almost unchanged up to $M \approx 10$. Only at higher M, central and side velocity peaks decrease as "magnetic braking" effects become significant, and the thickness of both the side and the Hartmann boundary layers decreases. A careful comparison of the w profiles shows that for $M >\sim 50$ the thickness of the Hartmann layers decrease roughly as M^{-1}, while the thickness of the side layers decreases less markedly, approximately as $M^{-1/2}$. These trends are in agreement with those amply reported in the literature for free or forced MHD flows in ducts (Moreau, 1990; Müller and Bühler, 2001), but the present study shows that they only apply to relatively high-Hartmann numbers, whereas the influence of MHD on velocity maxima and boundary layer thicknesses is much less marked at low values of M (< 50, say). This issue will be addressed on a more quantitative basis in Section 5, when results for the electrical currents are discussed.

The influence of the magnetic field on the convective velocities is summarized in Figure 8, which shows volume-averaged values of the velocity module $|\mathbf{v}|$ as a function of the Hartmann number in the whole range $M = 0-2000$ investigated. Values of $|\mathbf{v}|$ are normalized by the diffusive speed α/D, i.e. by a scale that does *not* depend upon the magnetic field. For moderate values of the Hartmann number, up to $M \approx 10$, velocities are little affected by MHD effects. For large M, mean velocities decrease roughly as M^{-2}, in agreement with classic results obtained by different authors for forced and buoyant MHD flows. An intermediate behavior is observed at intermediate Hartmann numbers (10–100).

Figure 9 shows alternative axonometric views of two particle trajectories for $M = 30$. The starting points are the same as in Figure 3, which was for $M = 0$ (no MHD). Trajectories were again split into two parts for the sake of clarity: graphs (a) and (b) are relative to the time interval $0 \leq t \leq 7.5\,D^2/\alpha^1$, graphs (c) and (d) to the subsequent interval $7.5\,D^2/\alpha^1 \leq t \leq 18\,D^2/\alpha^1$. As in the case of no MHD, the fluid moves from the front wall to the mid-plane $y/D = 0.5$ of the enclosure along lines close to the axes of the main circulation rolls, winds

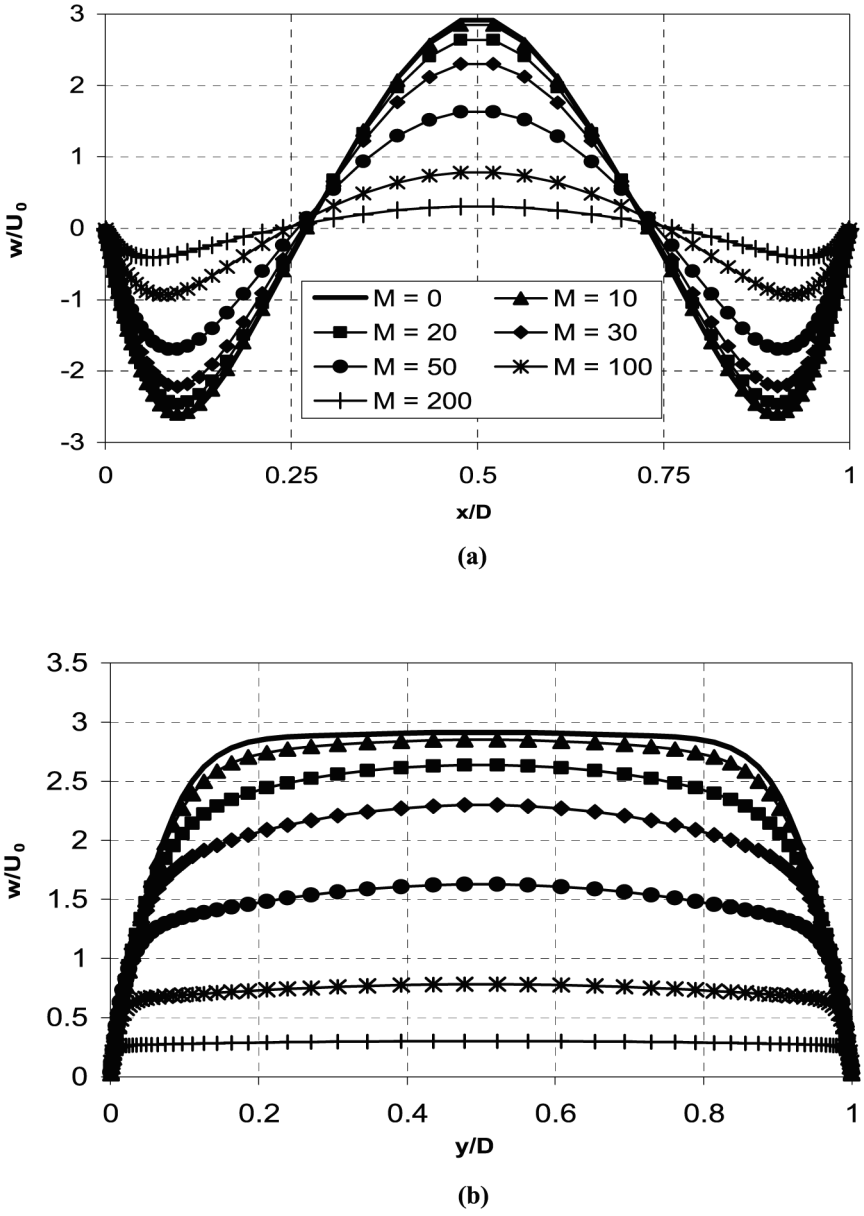

Figure 7.
Profiles of the vertical velocity w for different values of the Hartmann number. (a) profiles along x for $y/D = z/D = 0.5$; (b) profiles along y for $x/D = z/D = 0.5$. Values are normalized by the diffusive velocity scale $U_0 = \alpha/D$

outward and comes back towards the front wall in ample spirals. However, secondary velocities are now much lower than for the case $M = 0$, so that a longer time elapses, and both particles describe a much larger number of windings, before they approximately complete their cyclic path. For higher

Hartmann numbers, e.g. $M = 100$ or 1000, secondary velocities are so low that subsequent windings of the particles' trajectories practically coincide with one another and it is difficult to visualize overall paths similar to those in Figures 3 or 9.

Temperature distributions in the mid-plane $y/D = 0.5$ are shown in Figure 10 for four different values of the Hartmann number. As in Figure 4 ($M = 0$), temperatures are normalized by $(qD^2)/(8\lambda)$ (maximum conductive temperature). At low-Hartmann numbers, isotherms are but minimally distorted, as can be seen by comparing Figure 10(a) and (b) ($M = 10$ and 30) with Figure 4(a) ($M = 0$, i.e. no MHD). At higher values of M, e.g. $M = 100$ in Figure 10(c), vertical stratification is significantly suppressed. Finally, at very high-M, e.g. $M = 1000$ in Figure 10(d), a purely conductive temperature distribution is obtained, in which T is a function of the horizontal co-ordinate x only.

Figure 11 shows the distributions of the local heat flux q''_w along one of the side (thermally active) walls for the same above values of the Hartmann number. The distributions are, of course, identical on the two cold walls at $x = 0$ and $x = D$. The heat flux is normalized by its average value $qD/2$. As could be expected from the distributions of velocity and temperature, also the distribution of the wall heat flux is only negligibly affected by MHD effects at low M, compare Figure 11(a) ($M = 10$) with Figure 5(a) ($M = 0$). For higher Hartmann numbers, i.e. $M = 30$ and 100 in Figure 11(b) and (c), isoflux lines tend to align themselves with the horizontal direction while the heat flux peaking factor decreases from ~ 1.10 ($M = 0$, 10) to ~ 1.09 ($M = 30$) and ~ 1.04 ($M = 100$). Finally, at high-Hartmann numbers, e.g. $M = 1000$ in

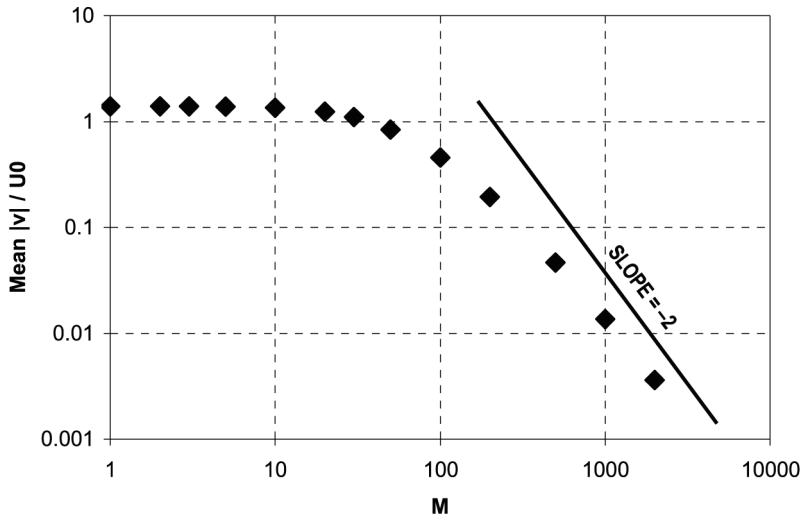

Figure 8.
Volume averaged values of the velocity module $|\mathbf{v}|$ as a function of the Hartmann number in the range $M = 0-2000$. Values of $|\mathbf{v}|$ are normalized by the diffusive velocity scale α/D

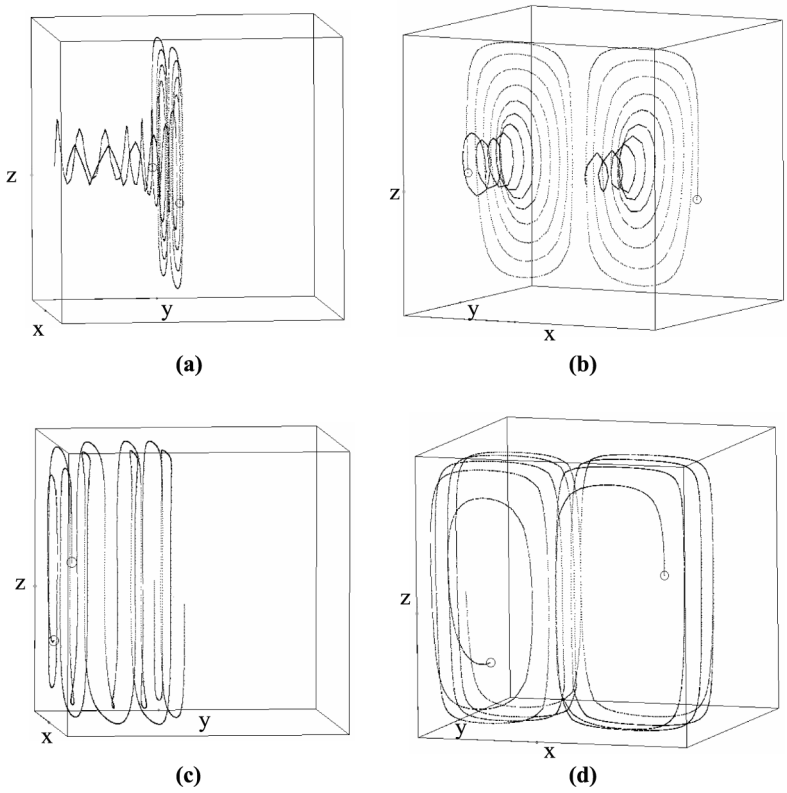

Figure 9.
Trajectories of two pseudo-particles for $M = 30$. (a, b) alternative axonometric views for $0 \le t \le 7.5 D^2 \alpha$; (c, d) alternative axonometric views for $7.5 D^2 \alpha^{-1} \le t \le 18 D^2 \alpha^{-1}$. The starting co-ordinates of the two particles are the same as in Figure 3 ($M = 0$), i.e. $x/D = 0.3$, $y/D = 0.05$, $z/D = 0.5$ (P1) and $x/D = 0.7$, $y/D = 0.05$, $z/D = 0.5$ (P2). Small circles indicate the final positions

Figure 11(d), the distribution of q''_w becomes practically flat, coherently with the purely conductive temperature distribution shown in Figure 10(d).

Distributions of the wall shear stress τ_w on one of the active walls ($x = 0$ or $x = D$) for different values of M are shown in Figure 12(a–d). The wall shear stress is normalized by ρU_0^2. The corresponding distribution for $M = 0$ was shown in Figure 5(b). As the Hartmann number increases, peaking factors for τ_w decrease from ~ 2 ($M = 0$) to just ~ 1.2 ($M = 1000$); at the same time, the regions of highest shear stress move downward until, for $M = 1000$, they practically coincide with the centers of the thermally active walls. Three-dimensional effects due to the influence of the orthogonal Hartmann walls remain significant up to the highest values of M investigated, and absolute values of τ_w (which are normalized here by a scale which does *not* depend on M) remain relatively high, since not only the near-wall velocity but also the thickness of the side layers decreases as M increases.

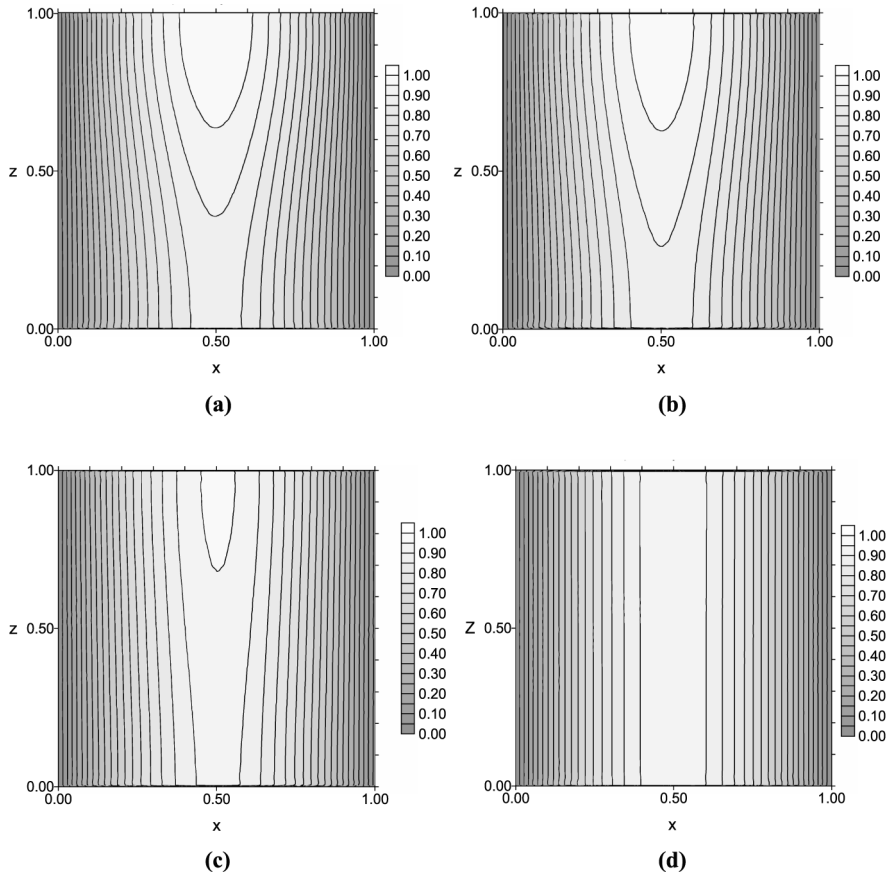

Figure 10.
Temperature distributions in the vertical mid-plane $y/D = 0.5$ of the enclosure for different values of the Hartmann number. (a) $M = 10$; (b) $M = 30$; (c) $M = 100$; (d) $M = 1000$. Temperatures are normalized by $(qD^2)/(8\lambda)$ (maximum conductive temperature)

5. Electrical currents and Hartmann layers

Figure 13 shows vector plots of the current density **J** on selected plane cross sections of the enclosure for the case $M = 10$ (low-Hartmann number). A reference vector, proportional to the reference current density $J_0 = (\mu\sigma)^{1/2}\alpha/D^2$, is shown; the same vector scaling was adopted for all four graphs in order to allow a better appreciation of the spatial distribution of **J**.

In particular, Figure 13(a) shows the horizontal mid-plane $z/D = 0.5$. Far from the Hartmann walls at $y = 0$ and D, the fluid rises throughout the whole central region of this cross section and descends along the side walls. The induced electric field $\mathbf{v} \times \mathbf{B}$ drives currents $\sigma\mathbf{v} \times \mathbf{B}$, which are directed from the right to the left in the central region of the plane, and from the left to the right in the side layers. These currents are only partly counteracted by diffusive terms $-\sigma\nabla\Phi$, in equation (5). In its turn, the interaction of overall currents with the

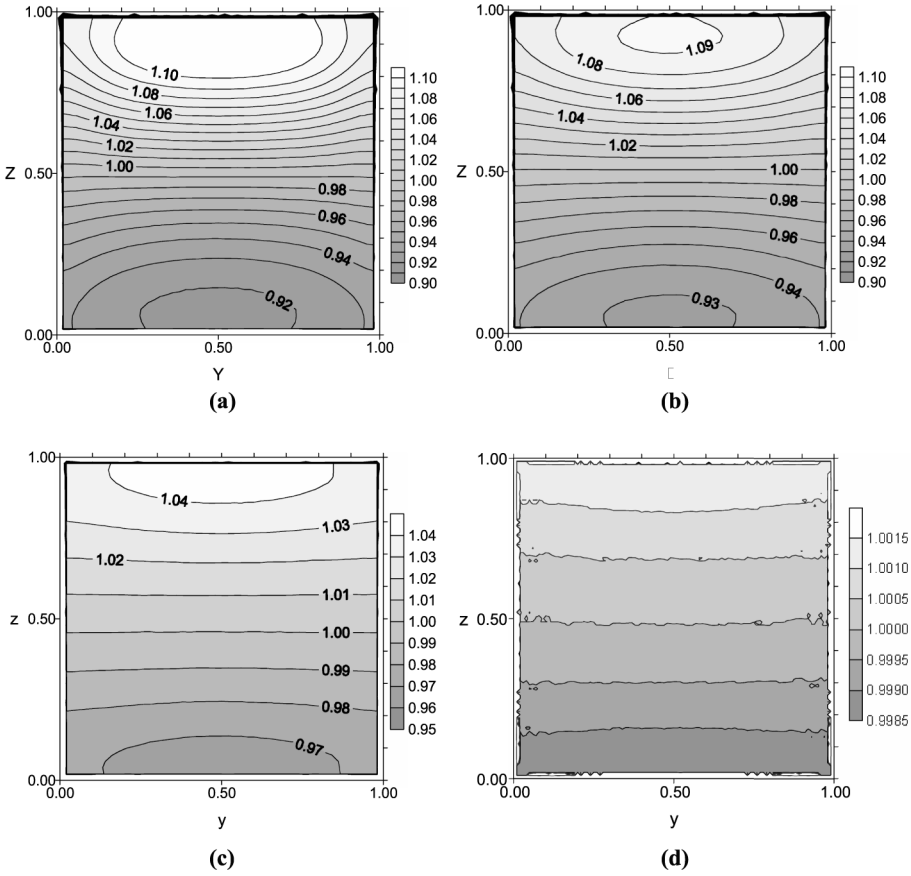

Figure 11. Distributions of the wall heat flux q''_w (normalized by $qD/2$) on one of the side (thermally active) walls for different values of the Hartmann number. (a) $M = 10$; (b) $M = 30$; (c) $M = 100$; (d) $M = 1000$. See Figure 5(a) for $M = 0$ (no MHD)

magnetic field **B** yields MHD forces $\mathbf{J} \times \mathbf{B}$, equation (3), which are almost everywhere opposite to the flow direction (braking forces). However, currents must close themselves somewhere; as Figure 13(a) shows, for the present moderate value of the wall conductance ratio c_w they do this mainly through the fluid itself in the Hartmann layers at $y \approx 0$ and $y \approx D$, which lie orthogonally to the direction of **B**. The result is that three distinct current loops, one central and two close to the side walls, can be observed in the proximity of each Hartmann wall. Note that only two side loops would be observed in the case of a differentially heated enclosure, as shown, for example, in Ciofalo and Cricchio (2001), their Figure 5. In the Hartmann layers, the MHD forces are aiding the main flow instead of braking against it, so that the fluid slips almost freely on these walls.

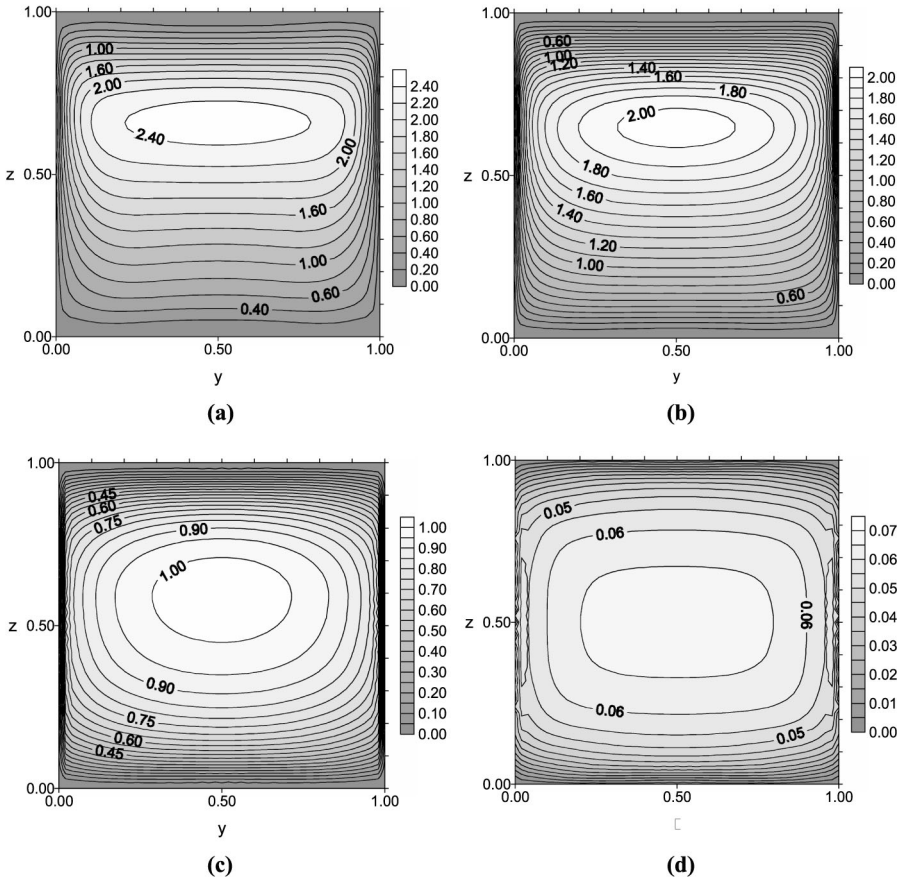

Figure 12.
Distributions of the wall shear stress τ_w (normalized by ρU_0^2) on one of the side (thermally active) walls for different values of the Hartmann number. (a) $M = 10$; (b) $M = 30$; (c) $M = 100$; (d) $M = 1000$. See Figure 5(b) for $M = 0$ (no MHD)

In this and in the following figures, it should be observed that, as anticipated in Section 2, the mid-plane $x/D = 0.5$ – which is a symmetry plane for the flow – is *not* a symmetry plane for the electric currents, which actually cross it. *Two* (approximate) symmetry planes for the electric currents do exist, but they are located at $x/D \approx 1/3$ and $x/D \approx 2/3$, i.e. staggered with respect to the flow symmetry plane.

The remaining graphs in Figure 13 show current density vector plots in cross sections parallel to the Hartmann walls. Figure 13(b) is for $y/D = 0.02$, i.e. well within the Hartmann layer. The near-wall current pattern, coherent with the above comments, can be appreciated. Currents attain here their highest values in the vertically intermediate region of the Hartmann layers, whereas they decrease near the top and bottom walls, in correspondance with

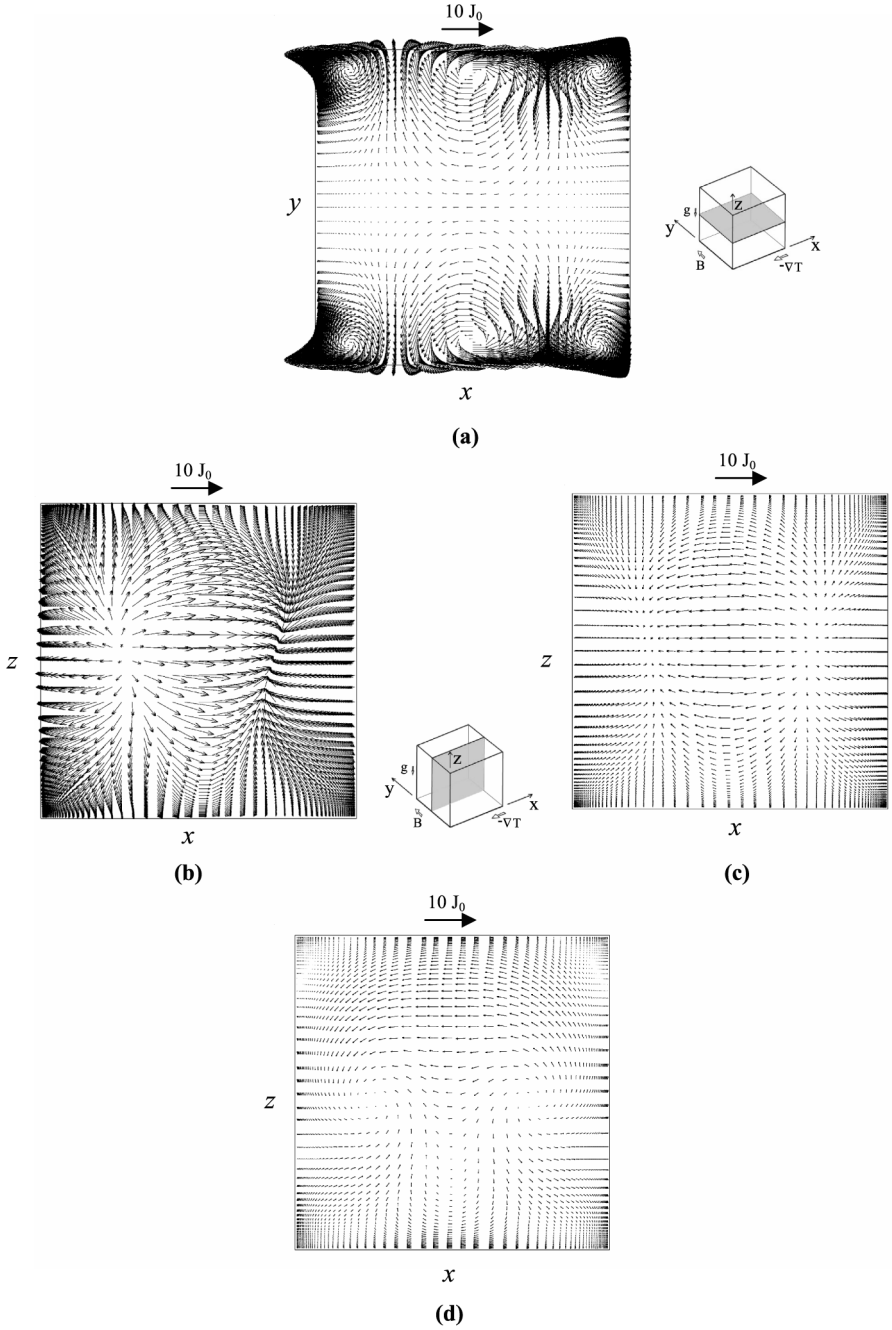

Figure 13.
Vector plots of the current density **J** on selected cross sections of the enclosure for $M = 10$. A reference vector, proportional to $J_0 = (\mu\sigma)^{1/2}\alpha/D^2$, is shown; all graphs are drawn using the same scale for vectors. (a) horizontal mid-plane $z/D = 0.5$; (b), (c), (d) constant-y planes parallel to the Hartmann walls: (b) $y/D = 0.02$, within the front Hartmann layer; (c) $y/D = 0.2$, in the core region; (d) $y/D = 0.5$, mid-plane

the turning of the fluid's velocity from horizontal to vertical or *vice versa*. Figure 13(c) is for the plane $y/D = 0.2$, which lies outside the Hartmann layer; currents are greatly reduced in size and follow a pattern opposite to that in the Hartmann layers, and typical of the core region. The dependance upon the vertical co-ordinate z remains about the same as in the near-wall region. Finally, Figure 13(d) is for the mid-plane $y/D = 0.5$; currents are even smaller in size than for $y/D = 0.2$, and exhibit a complex secondary pattern.

Figure 14 shows the same vector plots as Figure 13, but for a higher value of the Hartmann number ($M = 100$). Also the constant-y planes chosen for the current pattern visualization are different, so that the plane in graph (b) ($y/D = 0.01$) still lies within the Hartmann layer while that in graph (c) ($y/D = 0.1$) lies in the core region. The vector scale is the same for all four graphs and is identical to that used for $M = 10$ in Figure 13, so as to evidence the considerable increase in the current intensity obtained with respect to that lower Hartmann number.

The plot relative to the horizontal mid-plane $z/D = 0.5$, Figure 14(a), shows intense current "jets" near the corners where the Hartmann walls meet the side walls; these jets are similar to those predicted in previous work (Ciofalo and Cricchio, 2001) for the same geometry and a higher Rayleigh number, and can be correctly resolved only by adopting the present, fully resolved treatment of the Hartmann layers, whilst they are largely missed in numerical simulations based on the *ad hoc* coarse-grid treatment of these layers described in section. Current loops, in which the current density vectors turn from the direction followed in the core region to the opposite one characteristic of the Hartmann layers, are qualitatively similar, but much more intense, than those predicted for the lower Hartmann number (Figure 13), and have about the same extent. More generally, as will be discussed later, the thickness of the Hartmann layers is only slightly less than that observed for the much lower Hartmann number $M = 10$.

Also the current pattern in the cross section $y/D = 0.01$ lying within the front Hartmann layer, graph (b), is similar, but more intense, than the corresponding pattern reported in Figure 13(b) for $M = 10$. However, in the present case the pattern is almost perfectly symmetrical in the vertical direction, coherently with the reduced importance of inertial and buoyancy forces as compared with MHD effects. The current plot in the plane $y/D = 0.1$, graph (c), shows small upper and lower regions where the **J** direction is that typical of the Hartmann layers rather than that of the core region, which indicates that the thickness of the Hartmann layers increases above $0.1D$ in the proximity of the top and bottom walls.

Finally, corresponding current density vector plots are shown in Figure 15 for the high-Hartmann number case $M = 1000$. The cross sections in graphs (b) and (c), respectively, lying inside and outside of the front Hartmann layers, are located at $y/D = 0.001$ and $y/D = 0.01$ since the thickness of the Hartmann

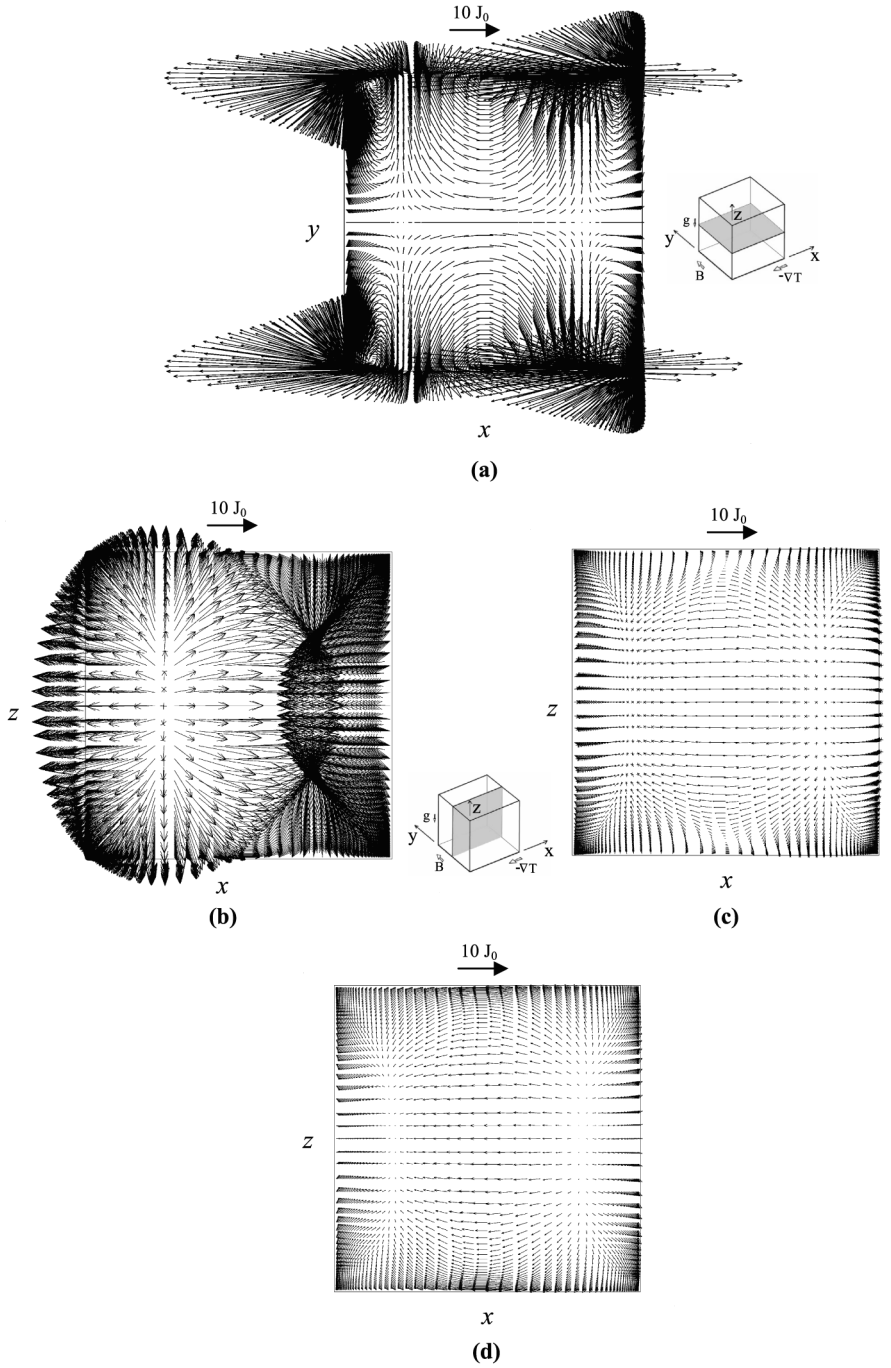

Figure 14.
Vector plots of the current density **J** on selected cross sections of the enclosure for $M = 100$. A reference vector, proportional to $J_0 = (\mu\sigma)^{1/2}\alpha/D^2$, is shown; all graphs are drawn using the same scale for vectors. (a) horizontal mid-plane $z/D = 0.5$; (b), (c), (d) constant-y planes parallel to the Hartmann walls: (b) $y/D = 0.01$, within the front Hartmann layer; (c) $y/D = 0.1$, in the core region; (d) $y/D = 0.5$, mid-plane

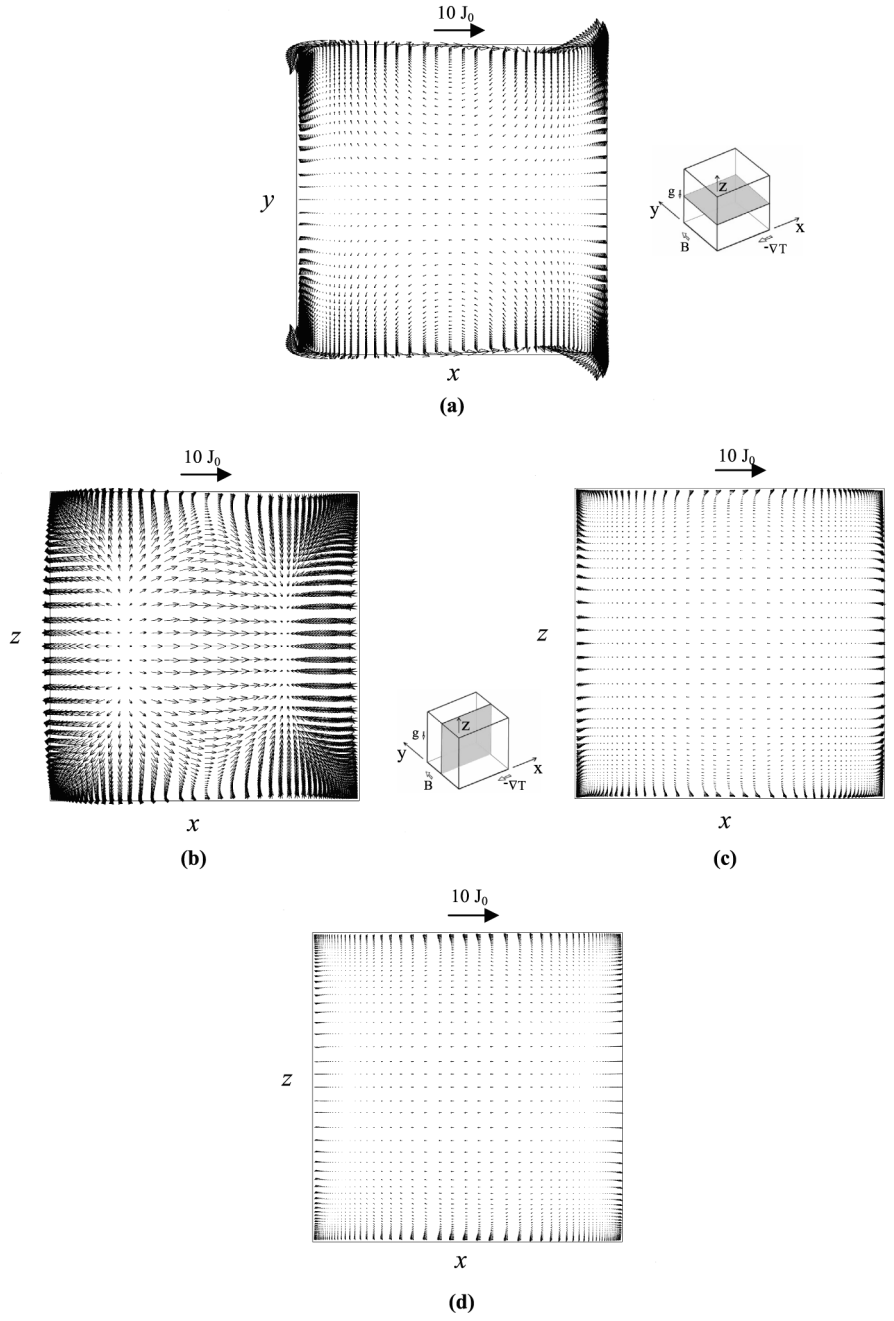

Figure 15.
Vector plots of the current density **J** on selected cross sections of the enclosure for $M = 1000$. A reference vector, proportional to $J_0 = (\mu\sigma)^{1/2}\alpha/D^2$, is shown; all graphs are drawn using the same scale for vectors. (a) horizontal mid-plane $z/D = 0.5$; (b), (c), (d) constant-y planes parallel to the Hartmann walls: (b) $y/D = 0.001$, within the front Hartmann layer; (c) $y/D = 0.01$, in the core region; (d) $y/D = 0.5$, mid-plane

layers is much lower than that in the previous cases $M = 10$ and $M = 100$. The scale used for the **J** vectors is the same as in the above two figures, which makes it evident how also current intensities are greatly reduced.

Figure 16 shows profiles of J_x (component of the current density vector **J** in the x direction) along the mid-line $x/D = z/D = 0.5$. For the purpose of clarity, only a few values of M are represented, and the graph is limited to the region $y/D \leq 0.1$ close to the front Hartmann wall. Of course, at very low values of M it is not completely appropriate to speak of Hartmann "layers" proper; here, however, these were *conventionally* identified with the near-wall regions where the sign of J_x is opposite to that observed in the core region away from the walls. Note that this is made possible by the moderate value of the conductance ratio ($c_w = 0.01$), which causes a large fraction of the electric currents to close themselves through the near-wall fluid; at much higher values of c_w, most of the currents would close through the solid wall and a fluid region of reversed J_x would not necessarily exist.

The thickness δ of the Hartmann layers, defined as discussed above, remains about the same ($\delta/D = 0.07$) for $M = 1$ and $M = 10$ and decreases significantly only for larger M. The current density, whose peaks are always attained at the Hartmann walls, reaches its maximum values for $M \approx 10-100$ and then decreases for larger M.

The dependence of the Hartmann layer thickness δ upon the Hartmann number M is summarized in Figure 17(a), which shows δ/D as a function of M in the whole range investigated. It is clear that δ remains about constant up to

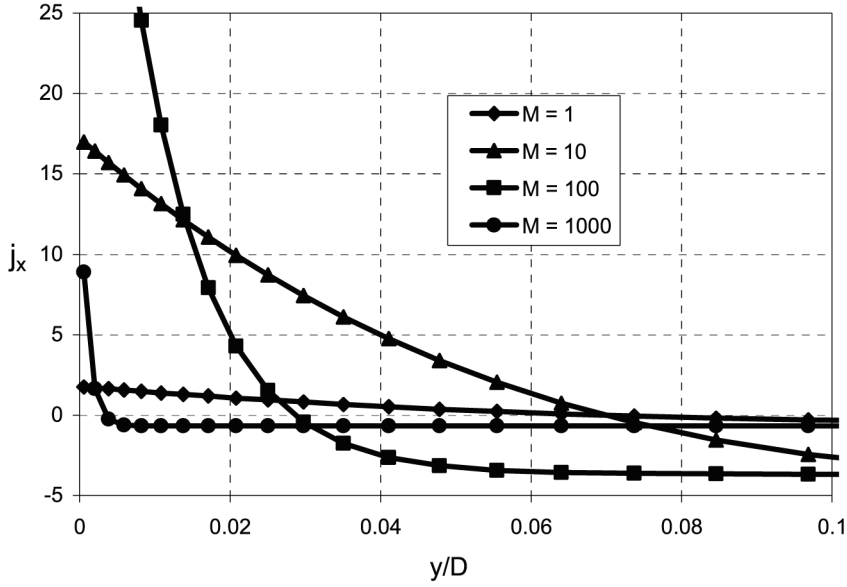

Figure 16.
Profiles of J_x (component of the current density vector **J** in the x direction) along the mid-line $x/D = z/D = 0.5$. Only a few values of M are represented, and the graph is limited to the region $y/D \leq 0.1$. The boundary between the Hartmann layer and the core region can be identified in each case by the inversion of the sign of J_x

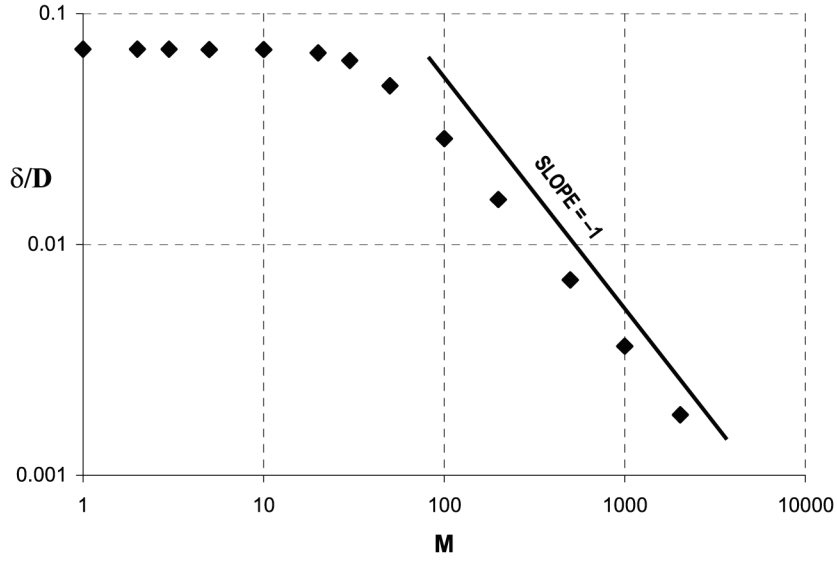

(a)

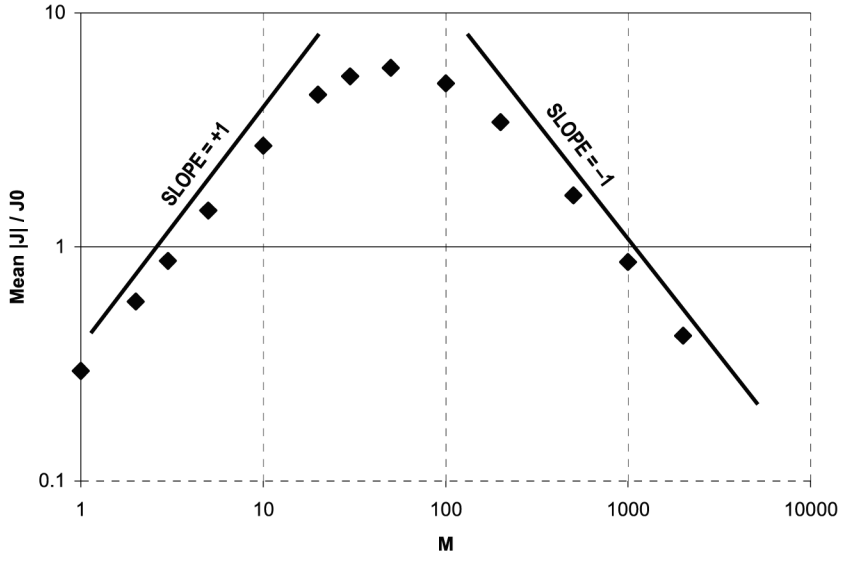

(b)

Figure 17.
Dependence of Hartmann layer thickness and mean current intensity on the Hartmann number in the whole range investigated.
(a) Hartmann layer thickness δ; (b) Volume-averaged value of the current density module $|\mathbf{J}|$

$M \approx 10$, then decreases and approaches the theoretical M^{-1} trend only in the limit of large M ($M > 100$, say). Figure 17(b) shows the volume-averaged value of the current density module $|\mathbf{J}|$ as a function of M. It shows that the mean current intensity increases about linearly with M for low-Hartmann numbers ($M < 10$), attains a maximum for $M \approx 50$ and approaches an M^{-1} trend in the limit of large M ($M > 100$).

6. Conclusions

Numerical simulations were performed for the magnetohydrodynamic free convection flow of a liquid metal in a cubic enclosure with volumetric heat generation under the influence of a horizontal magnetic field of different intensities. A finite volume code, purposely adapted to account for MHD effects, was used. The 64^3-volume computational grid adequately resolved the whole flow field including the Hartmann layers, so that both low-Hartmann number and high-Hartmann number conditions could be investigated without changing the grid or recurring to approximate, *ad hoc* treatments of the near-wall regions.

For Hartmann numbers M up to ~ 10, corresponding to values of the interaction parameter N up to ~ 3, the flow field was little affected by MHD effects. In this range, in which inertial forces dominate with respect to MHD forces, also the thickness δ of the Hartmann layers remained about uniform ($\delta/D = 0.07$) while electrical currents increased about linearly with M, i.e. with the intensity of the magnetic induction field.

At the opposite end of the range, i.e. for M larger than ~ 100 (corresponding to values of the interaction parameter N above ~ 300), MHD forces dominate and inertial forces become relatively unimportant. In this region velocities were found to decrease roughly as M^{-2} and current intensities roughly as M^{-1}. Also, the thickness of the Hartmann layers (as identified by the inversion in the direction of electrical currents) decreased approximately as M^{-1} and that of the side layers as $M^{-1/2}$. These trends are in agreement with the predictions of classic works on high-Hartmann number MHD flows in ducts, mainly derived under the assumption of negligible inertial terms.

In the intermediate range $M = 10$–100, the interesting result was obtained of the existence of a maximum for the intensity of electrical currents. This was attained at $M \approx 50$. The values of the fluid's speed and the thickness of the Hartmann and side layers exhibited an intermediate behavior between those described above for the two ends of the Hartmann number range investigated.

In several works on MHD buoyant flows, magnetohydrodynamic scales have been used to normalize velocities and electrical currents. For example, Bühler (1998) chose velocities and current scales which, in the present notation, can be expressed as $u_0 = U_0 \mathrm{Ra}/M^2$ and $j_0 = J_0 \mathrm{Ra}/M$, U_0 and J_0 being the corresponding scales adopted in the present paper. From the above discussion on the asymptotic trends of various quantities, it is clear that the adoption of

these magnetohydrodynamic scales yields constant values for the normalized velocities and electrical currents in the limit of very high values of the Hartmann number and of the interaction parameter. On the other hand, for low values of M this approach yields trends which are of little or no significance (for example, both velocities and currents would appear to increase as M^2 once normalized by the above scales u_0 and j_0, and current density maxima would not be observed). Moreover, both scales diverge for $M = 0$ and thus are not applicable to purely hydrodynamic flows, making incipient MHD effects more difficult to appreciate.

Finally, it should be stressed that the present results were obtained for specific (and rather moderate) values of the Rayleigh number and of the wall conductance ratio. While many of the above qualitative conclusions would remain valid for different values of Ra and c_w, the detailed results and the boundary values of M separating different MHD regimes would obviously change; further work will have to be done in order to clarify these issues.

References

AEA Technology, (2000), *CFX release 4.3 – User guide*, AEA Report, Harwell, UK.

Alboussière, T., Garandet, J.P. and Moreau, R. (1996), "Asymptotic analysis and symmetry in MHD convection", *Physics of Fluids*, Vol. 8 No. 8, pp. 2215-26.

Arcidiacono, S., Di Piazza, I. and Ciofalo, M. (2001), "Low-Prandtl number natural convection in volumetrically heated rectangular enclosures – II. Square cavity, $AR = 1$", *International Journal of Heat and Mass Transfer*, Vol. 44 No. 3, pp. 537-50.

Bühler, L. (1996), "Instabilities in quasi-two-dimensional magnetohydrodynamic flows", *Journal of Fluid Mechanics*, Vol. 326, pp. 125-50.

Bühler, L. (1998), "Laminar buoyant magnetohydrodynamic flow in vertical rectangular ducts", *Physics of Fluids*, Vol. 10 No. 1, pp. 223-36.

Burns, A. and Wilkes, N. (1987), *A Finite Difference Method for the Computation of Fluid Flow in Complex Three-dimensional Geometries*, UKAEA Report AERE – R 12342, Harwell, UK.

Ciofalo, M. and Collins, M.W. (1989), "k-ε Predictions of heat transfer in turbulent recirculating flows using an improved wall treatment", *Numerical Heat Transfer*, Vol. 15, pp. 21-47 Part B.

Ciofalo, M. and Cricchio, F. (2001), "Numerical simulation of MHD fully developed buoyant flow at low *Pr*: 'direct' vs 'ad hoc' treatment of the Hartmann layers", *Proc. 19th UIT National Heat Transfer Conference*, pp. 439–444.

Ciofalo, M. and Cricchio, F. (2002), "Computation of MHD buoyant flows at low-Prandtl number in a cubic enclosure", To be presented at the 12th International Heat Transfer Conference, Grenoble, France.

Di Piazza, I. "Prediction of free convection in liquid metals with internal heat generation and/or magnetohydrodynamic interactions", Doctoral Thesis in Nuclear Engineering, University of Palermo, Italy.

Di Piazza, I. and Bühler, L. (2000), "A general computational approach for magnetohydrodynamic flows using the CFX code: buoyant flow through a vertical square channel", *Fusion Technology*, Vol. 38 No. 2, pp. 180-9.

Di Piazza, I. and Ciofalo, M. (2002a), "MHD free convection in a liquid-metal filled cubic enclosure – I. Differential heating", *International Journal of Heat and Mass Transfer*, Vol. 45 No. 7, pp. 1477-92.

Di Piazza, I. and Ciofalo, M. (2002b), "MHD free convection in a liquid-metal filled cubic enclosure – II. Internal heating", *International Journal of Heat and Mass Transfer*, Vol. 45 No. 7, pp. 1493-511.

Henkes, R.A.W.M. and Le Quéré, P. (1996), "Three-dimensional transition of natural-convection flows", *Journal of Fluid Mechanics*, Vol. 319, pp. 281-303.

Kightley, J.R. (1985), *The conjugate gradient method applied to turbulent flow calculations*, UKAEA Report CSS 184 (HL85/1584), Harwell, UK.

Leboucher, L. (1995), *Numerical simulation of unsteady magnetohydrodynamic flows in ducts*, Technical Report FZKA 5663, Forschungszentrum Karlsruhe, Germany.

Leboucher, L. (1999), "Monotone scheme and boundary conditions for finite volume simulation of magnetohydrodynamic internal flows at high Hartmann number", *Journal of Computational Physics*, Vol. 150, pp. 181-98.

Leonard, B.P. (1979), "A stable and accurate convective modelling procedure based on quadratic upstream interpolation", *Computer Methods in Applied Mechanics and Engineering*, Vol. 19, pp. 59-98.

Malang, S., Tillack, M.S., (Eds) (1995), *Development of Self-cooled Liquid Metal Breeder Blankets*, Technical Report FZKA 5581, Forschungszentrum Karlsruhe, Germany.

Mallinson, G.D. and de Vahl Davis, G. (1977), "Three-dimensional natural convection in a box: a numerical study", *Journal of Fluid Mechanics*, Vol. 83, pp. 1-31.

Moreau, R. (1990), *Magnetohydrodynamics*, Kluwer Academic Publisher, Amsterdam.

Müller, U. and Bühler, L. (2001), *Magnetofluiddynamics in channels and containers*, Springer, Wien, New York.

Proust, E., Anzidei, L., Casini, G., Dalle Donne, M., Giancarli, L. and Malang, S. (1993), "Breeding blanket for DEMO", *Fusion Engineering and Design*, Vol. 22, pp. 19-33.

Rhie, C.M. and Chow, W.L. (1983), "A numerical study of the turbulent flow past an aerofoil with trailing edge separation", *AIAA Journal*, Vol. 21, pp. 1525-32.

Stone, H.L. (1968), "Iterative solution of implicit approximations of multidimensional partial differential equations", *SIAM Journal of Numerical Analysis*, Vol. 5, pp. 530-58.

Tagawa, T. and Ozoe, H. (1997), "Enhancement of heat transfer rate by application of a static magnetic field during natural convection of liquid metal in a cube", *ASME Journal of Heat Transfer*, Vol. 119, pp. 265-71.

Tagawa, T. and Ozoe, H. (1998a), "Enhanced heat transfer rate measured for natural convection in liquid gallium in a cubical enclosure under a static magnetic field", *ASME Journal of Heat Transfer*, Vol. 120, pp. 1027-32.

Tagawa, T. and Ozoe, H. (1998b), "The natural convection of liquid metal in a cubical enclosure with various electro-conductivities of the wall under the magnetic field", *International Journal of Heat and Mass Transfer*, Vol. 41, pp. 1917-28.

Van Doormal, J.R. and Raithby, G.D. (1984), "Enhancements of the SIMPLE method for predicting incompressible flows", *Numerical Heat Transfer*, Vol. 7, pp. 147-63.